Grain Size Sensitive Creep During Simulated Seismic Slip in Nanogranular Fault Gouges: Constraints From Transmission Kikuchi Diffraction (TKD)

Matteo Demurtas[1,2] [iD], Steven A. F. Smith[2], David J. Prior[2] [iD], Frank E. Brenker[3], and Giulio Di Toro[4,5] [iD]

[1]Physics of Geological Processes, The Njord Centre, Department of Geosciences, University of Oslo, Oslo, Norway, [2]Department of Geology, University of Otago, Dunedin, New Zealand, [3]Geosciences Institute, Goethe University Frankfurt, Frankfurt, Germany, [4]Istituto Nazionale di Geofisica e Vulcanologia, Rome, Italy, [5]Dipartimento di Geoscienze, Università degli Studi di Padova, Padova, Italy

Abstract Nanograins ($\ll 1$ μm) are common in the principal slip zones of natural and experimental faults, but their formation and influence on fault mechanical behavior are poorly understood. We performed transmission Kikuchi diffraction (spatial resolution 20–50 nm) on the principal slip zone of an experimental carbonate gouge (50 wt% calcite, 50 wt% dolomite) that was deformed at a maximum slip rate of 1.2 m/s for 0.4 m displacement. The principal slip zone (PSZ) consists of nanogranular aggregates of calcite, Mg-calcite, dolomite and periclase, dominated by grain sizes in the range of 100–300 nm. Nanograins in the ultrafine (< 800 nm) PSZ matrix have negligible internal lattice distortion, while grains > 800 nm in size contain subgrains. A weak crystallographic preferred orientation is observed as a clustering of calcite *c*-axes within the PSZ. The high-resolution microstructural observations from transmission Kikuchi diffraction, in combination with published flow laws for calcite, are compatible with high-velocity slip in the PSZ having been accommodated by a combination of grain size sensitive creep in the ultrafine matrix, and grain size insensitive creep in the larger grains, with the former process likely controlling the bulk rheology of the PSZ after dynamic weakening. If the activation energy for creep is lowered by the nanogranular nature of the aggregates, this could facilitate grain size sensitive creep at high (coseismic) strain rates and only moderate bulk temperatures of approximately 600 °C, although temperatures up to 1000 °C could be locally achieved due to processes such as flash heating.

1. Introduction

Nanograins ($\ll 1$ μm) are widely reported in both natural (e.g., Chester et al., 2005; Demurtas et al., 2016; Ma et al., 2006; Novellino et al., 2015; Pittarello et al., 2008; Siman-Tov et al., 2013; Smeraglia et al., 2017; Wilson et al., 2005) and experimental fault slip zones (e.g., Yund et al., 1990; Han et al., 2007, 2010; Reches & Lockner, 2010; De Paola et al., 2011; Han et al., 2011; Tisato et al., 2012; Chen et al., 2013; Verberne et al., 2013, 2014; De Paola et al., 2015; Green et al., 2015; Spagnuolo et al., 2015; Yao et al., 2016; Aretusini et al., 2017; Smeraglia et al., 2017; Pozzi et al., 2018, 2019). Hypotheses for the formation of nanograins in faults include (i) thermal decomposition (e.g., Green et al., 2015; Han et al., 2007), (ii) dynamic rock pulverization (Wilson et al., 2005) and milling (Siman-Tov et al., 2013), (iii) shock-like stress release associated with migration of fast-moving dislocations (Spagnuolo et al., 2015), (iv) subcritical crack growth in compression (Sammis & Ben-Zion, 2008), and (v) crack nucleation and propagation under high tensile strain rates (Sammis & Ben-Zion, 2008).

Nanograins have been generated in rock deformation experiments simulating both aseismic and coseismic deformation conditions (e.g., Han et al., 2010; Tisato et al., 2012; Verberne et al., 2013; Spagnuolo et al., 2015; Smeraglia, Bettucci, et al., 2017, Pozzi et al., 2018, 2019). In the low-velocity, aseismic regime ($v \leq 100$ μm/s), microstructural observations of calcite gouges indicated that nanograins can be generated by plastic deformation, fracturing, and abrasion, and that they subsequently deform by grain boundary sliding aided by either dislocation or diffusion creep (Verberne et al., 2014). Verberne et al. (2014) documented sintering between the nanograins leading to the development of nanofibers that likely deformed by a granular flow mechanism, with competition between dilation caused by grain-neighbor swapping and

compaction due to active diffusive mass transfer. In their case, the presence of a crystallographic preferred orientation (CPO) within shear bands cutting the gouge was interpreted to be the result of cataclastic flow aided by shear-induced dislocation glide at the grain contacts (Verberne et al., 2013).

High-velocity ($v > 0.1$ m/s) rock friction experiments aimed at reproducing seismic deformation conditions introduced the term "powder lubrication" to describe the production of nanograins in slip zones and the concomitant dynamic fault weakening (e.g., Han et al., 2010; Han et al., 2011; Reches & Lockner, 2010; Tisato et al., 2012). However, dynamic weakening may not be directly related to the formation of nanograins. More recent experimental studies have explored the possibility that nanograins could influence fault rheological properties due to the activation of "viscous" deformation mechanisms at high slip velocity (De Paola et al., 2015; Pozzi et al., 2018, 2019). In particular, the production of nanograins coupled with temperature rise due to frictional heating could promote grain size sensitive deformation mechanisms such as grain boundary sliding accompanied by dislocation or diffusion creep (i.e., superplastic flow in the broad sense; Schmid et al., 1977), which may lead to efficient strain accommodation and dynamic weakening at high velocities (De Paola et al., 2015; Green et al., 2015; Spagnuolo et al., 2015; Pozzi et al., 2018, 2019). Microstructural investigation of experimental slip zones showed the presence of equant nanograins (from 10 to 600 nm in size) forming a foam-like fabric with abundant grain triple junctions and a low dislocation density (De Paola et al., 2015; Green et al., 2015; Spagnuolo et al., 2015). The occurrence of similar microstructures has been associated with superplastic flow, defined as the ability of materials to accommodate unusually high strains without complete necking (Boullier & Gueguen, 1975; Fliervoet et al., 1999; Poirier, 1985; Walker et al., 1990).

Despite this recent progress in understanding the formation and role of nanograins during faulting, the deformation mechanisms active in nanogranular slip zones are still poorly understood, partly because of the difficulty in characterizing the microstructural and crystallographic properties of nanogranular materials. Microstructural studies and interpretation of deformation mechanisms within nanograin aggregates have relied mainly on scanning (SEM) and transmission electron microscope (TEM) analyses. Limitations with the spatial resolution of conventional electron backscatter diffraction (EBSD) on geological materials (approximately 50 to 250 nm depending on the material; Humphreys & Brough, 1999; Prior et al., 1999, 2009) has hindered application of EBSD to the study of nanograins. Recently, Pozzi et al. (2019) successfully applied EBSD to the study of nanogranular slip zones in experimentally deformed calcite gouges, and were able to resolve grains as small as 500 nm in size (step size of the analysis 200 nm). However, natural and experimental slip zones often contain grains that are tens to hundreds of nanometers in size, hence too small to be properly resolved using conventional EBSD (e.g., De Paola et al., 2015; Green et al., 2015). Although TEM has a spatial resolution of $\ll 1$ nm, the study area with TEM is often less than a few tens of square micrometers, and therefore, crystallographic data sets are often limited to a few grains. As a consequence, the collection of statistically significant data sets concerning the crystallography of grain aggregates is time consuming and challenging using TEM.

Transmission Kikuchi diffraction (TKD) is a SEM-based technique that can provide similar crystallographic data to conventional EBSD, but at a significantly higher spatial resolution (i.e., up to 1–2 nm in metal alloys; Keller & Geiss, 2012; Trimby, 2012; Trimby et al., 2014). Application of TKD to geological samples is still in its infancy, but recent studies have shown that TKD can be applied successfully to study nanogranular geological materials including diamonds and sheared travertines (i.e., Delle Piane et al., 2018; Piazolo et al., 2016). In this study, we applied TKD to a nanogranular principal slip zone (PSZ) that was produced in a high-velocity shear experiment on calcite-dolomite gouges. We use the nanostructural observations to test current hypotheses regarding deformation mechanisms that are potentially active during seismic faulting in carbonates.

2. Materials and Methods

The TKD analysis was performed on a sample of deformed gouge composed of 50 wt% calcite and 50 wt% dolomite (Figure 1). The calcite-dolomite mixture was obtained by crushing Carrara marble (99.9% calcite) and dolomitized Calcare Massiccio (99% dolomite) from the damage zone of the Vado di Corno Fault Zone (Demurtas et al., 2016). The powders were passed through a 250 μm sieve and then mixed together by slow tumbling for approximately 30 min. The gouge was deformed in a rotary-shear apparatus (Slow-to High-Velocity rotary-shear Apparatus; Di Toro et al., 2010; Niemeijer et al., 2011; Smith et al., 2013) at
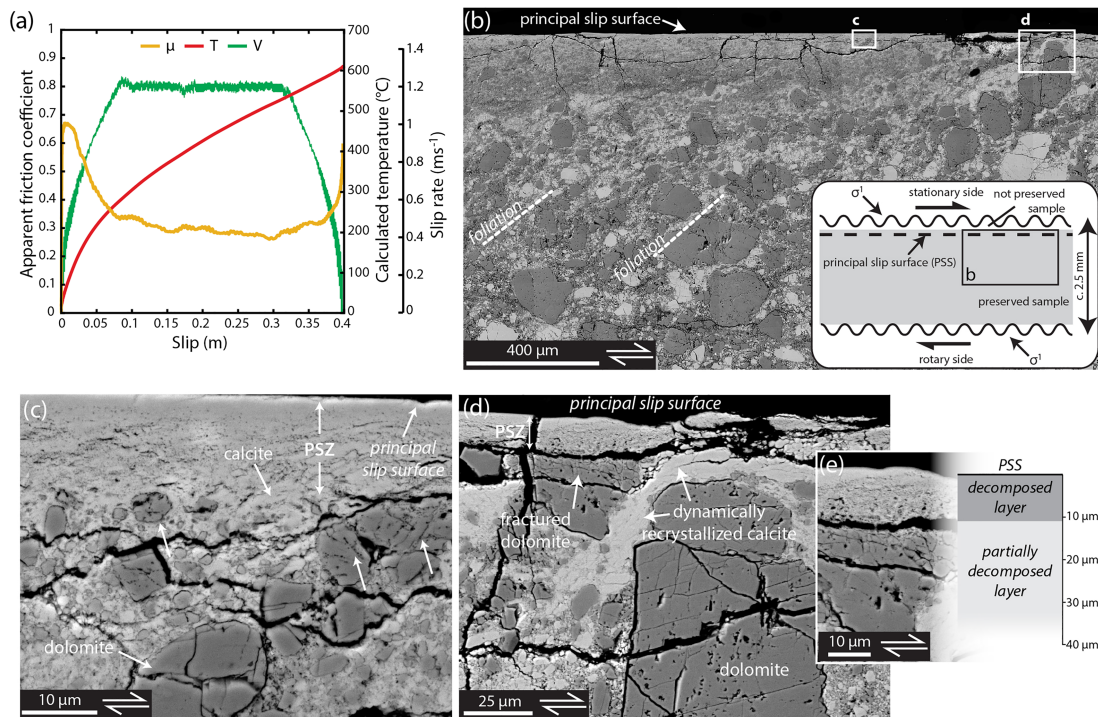
Figure 1. Mechanical data and microstructures of experiment *s1221*. (a) Evolution of apparent friction coefficient (μ, orange), slip velocity (v, green), and estimated temperature rise (T, red). (b) SEM image of the bulk gouge layer showing a foliation and a discrete principal slip surface (Smith et al., 2017). Inset shows the overall sample geometry and location of area shown in the main image. (c) SEM image of the highly localized PSS and adjacent PSZ with dolomite grains showing evidence of thermal decomposition (i.e., intragranular porosity and vesicular rims). (d) SEM image of patches of dynamically recrystallized calcite and vesicular dolomite adjacent to the PSZ. (e) Magnification from (d) of the PSZ transitioning to a partially thermally decomposed dolomite clast.

a peak slip velocity of 1.2 m/s for 0.4 m of displacement (Figure 1a; experiment *s1221* in Demurtas et al., 2019). The experiment was performed in room-humidity conditions (room temperature of 20 °C and room humidity of 49%) at a constant normal stress of 17.5 MPa (Figure 1a). Following the experiment, the principal slip surface (PSS) and adjacent PSZ were extracted and embedded in low-viscosity epoxy. Estimates of temperature rise during shearing were obtained by applying the mathematics of Rice (2006), assuming that the principal slip surface can be treated as a plane of zero thickness (supporting information).

Sample preparation for TKD was carried out by Argon Ion Slicing following the methods outlined in Stojic and Brenker (2010; Figure 2). The Argon Ion Slicing procedure produces a large ($2-4 \times 10^4 \ \mu m^2$) electron-transparent area along the leading edge of the sample, which in our case corresponds to the region containing the PSS and PSZ that formed during high-velocity shearing (Figure 2).

The TKD data were collected on a Zeiss Sigma VP Field-Emission-Gun SEM equipped with a NordlysF EBSD camera from Oxford Instruments, located at the Otago Centre for Electron Microscopy, University of Otago (New Zealand). The TKD patterns were indexed and processed using Oxford Instruments AZtec software. The sample was mounted on a microclamp SEM substage fixed to a standard SEM sample holder and back-tilted 3.3° from horizontal (supporting information). The sample was kept at a working distance of 8 mm and the SEM operated at an accelerating voltage of 30 kV and a beam aperture of 120 μm. Analysis was performed under variable pressure conditions and charging was avoided by maintaining a few pascals of nitrogen inside the chamber. Given the sufficiently similar geometry of the TKD analysis to EBSD, the estimated angular resolution for TKD analysis was of ± 0.5° (measured on a Si standard).

The electron transparent area in the thinned sample is located between 1.2 and 27.75 μm from the PSS (Figures 2a–2c). Microstructural observations and compositional analyses (i.e., X-ray powder diffraction analysis) suggest that this part of the gouge layer accommodated most of the strain during deformation, and that the dolomite within this layer experienced thermal decomposition (Figures 1c, 1d, and 3). For X-ray powder diffraction analysis, intact pieces of the cohesive PSZ were recovered after the experiment and the analysis
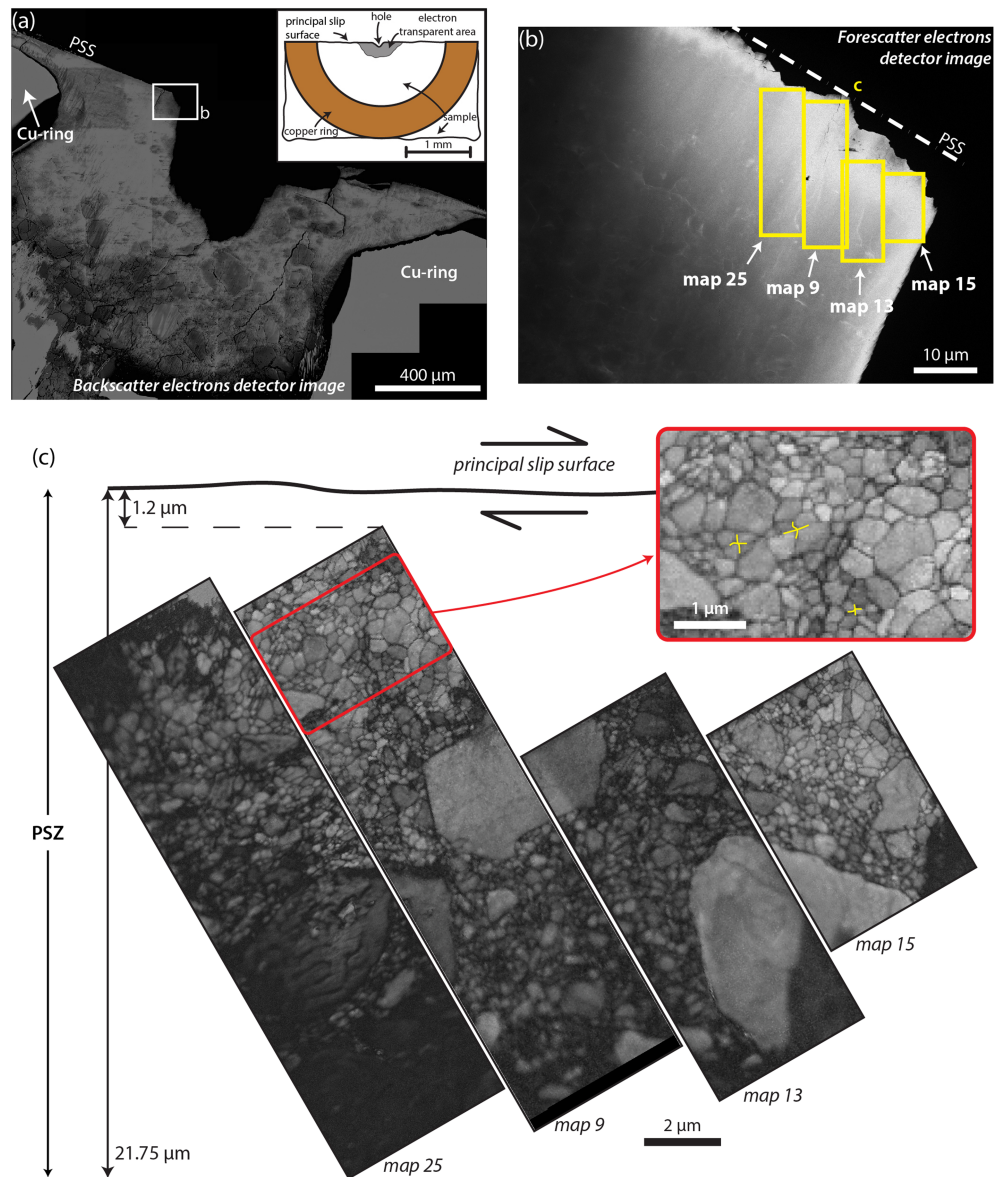
Figure 2. Sample preparation and analysis. (a) SEM backscatter electron image of the electron transparent sample prepared with ArIS. Inset shows a cartoon of the sample geometry. (b) Forescatter electron detector image of the analyzed area. Yellow boxes show the location of the four TKD maps. (c) Four band contrast maps from TKD analysis. The PSZ contains polygonal nanograins with a foam-like microstructure. Inset shows occurrence of quadruple junctions at grain boundaries in the upper part of *map 9*.

was performed directly on the polished PSS, without any grinding or separation, at the Department of Geosciences, University of Padova (Italy). Four adjacent TKD maps were collected at a step size of 20–50 nm, covering a total area of 477 μm^2 (Figures 2b and 2c; approximately 22 × 22 μm). Although this area is small compared to the total dimensions of the sample, SEM analysis indicate that the microstructures targeted with TKD are representative of the general microstructure of the PSZ (i.e., ultrafine-grained recrystallized layer adjacent to the PSS; see Figures 1c and 1d and section 3.2 below). Therefore, our TKD observations and data can be interpreted as representative of similar areas within the PSZ. The TKD patterns were stored, allowing the quality of indexing to be improved in the postprocessing stage (see supporting information for details on the data postprocessing). Grains were constructed from raw TKD data using the Voronoi decomposition in the open-source MTEX toolbox for MATLAB (Bachmann et al., 2011). Grains were defined as being surrounded by boundaries with a misorientation angle of > 10°.
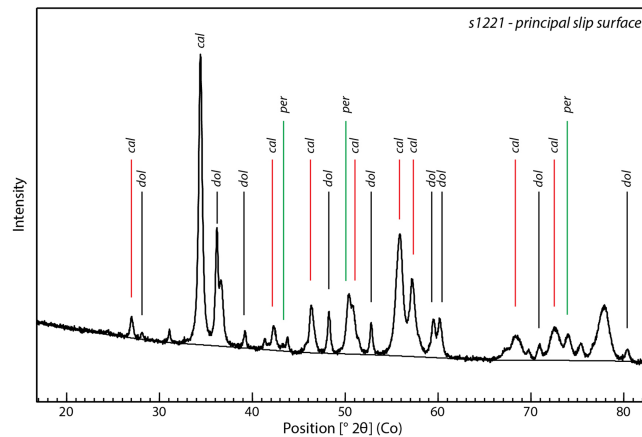
Figure 3. XRPD analysis on the principal slip surface of experiment *s1221*. The PSS is composed of dolomite (*dol*, black lines), Mg-calcite (*cal*, red lines), and periclase (*per*, green lines).

Grains composed of fewer than 10 pixels were ignored to avoid artifacts. Orientation data were plotted as stereoplots and contoured using the Orientation Density Function (after Bunge, 1982; Bachmann et al., 2010). The Orientation Density Function was calculated using a de la Vallee Poussin kernel, a half-width of 10°, and accounting for one point per grain. All pole figures were plotted as equal area and upper hemisphere.

For analysis of grain sizes and shapes, grain boundaries were hand-traced from band contrast images (Figure 2c). The analysis was performed in Image SXM, excluding grains touching the border of the maps (Figure 4; Barrett, 2015). Grain size was calculated as the diameter of an area-equivalent circle. Grain shape-preferred orientation was calculated for the best fit ellipses of grains with an aspect ratio ≥ 1.5. Angles in this paper are counterclockwise from the PSS.

3. Results

3.1. Mechanical Behavior and Temperature Rise in the Gouge Layer

The mechanical behavior of the calcite-dolomite gouge is consistent with previous studies (e.g., Smith et al., 2017). The gouge shows an initial increase of the apparent friction coefficient ($\mu = 0.68$) followed by dynamic weakening to reach a steady state friction coefficient of $\mu = 0.28$ (Figure 1a). During deceleration at the end of the experiment, the friction coefficient increases to $\mu = 0.56$ (Figure 1a). Calculations of the temperature rise suggest that the PSS reached a temperature of approximately 620 °C, which is consistent with thermocouple measurements of temperature increase in the adjacent PSZ (supporting information). Additionally, X-ray powder diffraction analysis performed on the principal slip surface shows the presence of periclase, one of the products of the thermal decomposition of dolomite above temperatures of approximately 550 °C (i.e., $CaMg(CO_3)_2 \rightarrow CaCO_3 + MgO + CO_2$; Samtani et al., 2002), along with dolomite and Mg-calcite (Figure 3).
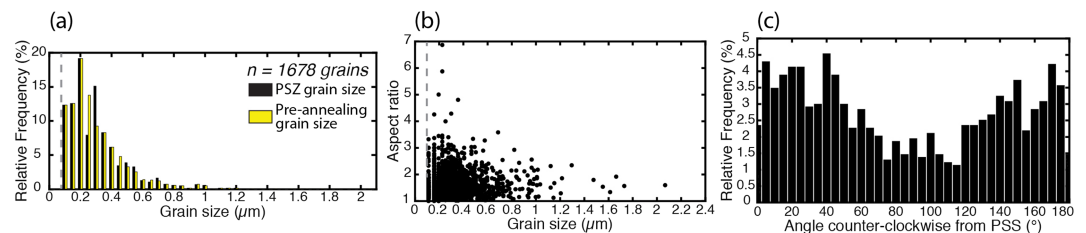
Figure 4. Grain size and shape analysis. (a) Grain size distribution calculated from band contrast images (black bars) and the calculated initial grain size distribution before annealing (yellow bars). The dashed line at 100 nm corresponds to the lower grain size threshold. (b) Plot of aspect ratio versus grain size. (c) Orientation distribution of the long axes of grains with an aspect ratio > 1.5.

3.2. Microstructures of the Principal Slip Zone

The bulk gouge is characterized by a well-developed foliation defined by alternating calcite- and dolomite-rich domains oriented at ~40° to the PSS (Figure 1b; similar to Smith et al., 2017). The PSZ consists of a continuous 15–20 μm thick, ultrafine-grained layer (≪ 1 μm in size; Figures 1c–1e) composed of calcite, Mg-calcite, and periclase (Figure 3). Adjacent to the PSZ, a ~30–40 μm thick layer includes dolomite grains with clusters of small holes and vesicular rims, interpreted to form by degassing during dolomite decarbonation (Figures 1c–1e; Mitchell et al., 2015). Elongate patches of recrystallized calcite are observed adjacent to the PSZ (Figure 1d).

Band contrast maps derived from TKD show that grains in the PSZ are polygonal and roughly equant (typical aspect ratio < 2.5; Figures 2c and 4b). Areas characterized by high-quality data (i.e., lighter areas in Figure 2c) show a compact recrystallized PSZ with negligible porosity. Grain boundaries are commonly straight to slightly curved (Figure 2c). Grains meet at 120° triple junctions, and quadruple junctions are also common (Figure 2c).

Figure 4a shows the results of grain size analysis. Grains <100 nm in size are not included in the data set due to the lower resolution of the TKD analysis (i.e., 20 to 50 nm). Overall, the grain size distribution shows a range of grain sizes up to 2068 nm and a median value of 252 nm. The largest grains are composed of dolomite and are embedded within an ultrafine calcite-rich recrystallized matrix (Figures 1c and 1d). The matrix shows one main population of grains with a peak centered at approximately 200–300 nm (Figure 4a). Analysis of the shape-preferred orientation of all grains shows two weak preferred orientations with grain long axes oriented at approximately 40° and approximately 150° from the PSS (Figure 4c).

### 3.3. Crystallographic Preferred Orientation and Intragranular Misorientation in Nanograins

Significant variation in the CPO is observed in the four different TKD maps. In *maps 25* and *9*, calcite shows two main clusters of (0001) oriented at 20–45° to the *y*-axis (Figure 5). Multiple clustering is observed on $\overline{1}\overline{1}20$ and $\{10\overline{1}4\}$, whereas on $\{01\overline{1}8\}$, the CPO is similar, but weaker, than that observed on (0001). In *map 13*, *c*-axes are organized into two clusters located near the circumference of the pole figure and aligned subparallel to the *y*-axis (Figure 5). There is no preferred alignment of the other crystallographic planes and directions. Finally, *map 15* is characterized by four weakly defined clusters of (0001) and multiple clustering on the other crystallographic planes and directions (Figure 5).

Grains in the ultrafine matrix (grain size < 800 nm) display low to negligible intragranular misorientation (< 1–2°; Figure 6a). Conversely, grains larger than approximately 800 nm contain subgrains with low-angle boundaries (misorientation angle < 10°; Figure 6b). Subgrains have roughly the same size as strain-free grains in the surrounding matrix.

4. Discussion

Microstructural data collected by TKD allow us to explore the deformation mechanisms that are potentially active during slip at high velocities, equivalent to those experienced during localized coseismic slip in natural faults (Rowe & Griffith, 2015). Recent work by De Paola et al. (2015) and Pozzi et al. (2018, 2019) on calcite gouges suggested a progressive transition from brittle deformation to viscous flow accompanying dynamic weakening and temperature increase at high slip velocities. During the initial slip-strengthening phase, the gouge deforms mainly by cataclasis aided by twinning, resulting in the progressive development of a comminuted and fine-grained shear band (Beeler et al., 1996; Smith et al., 2015). During dynamic weakening, the temperature increase in the principal slip zone activates both grain size sensitive (GSS) and insensitive (GSI) creep mechanisms, accompanying a dramatic decrease in shear stress. Once the shear stress on the fault has dropped to a steady state, GSS creep is dominant, and may weaken any CPO that had previously formed due to GSI creep.

Static grain growth during cooling at the end of this type of high-velocity experiment potentially modifies the grain size distribution and grain shapes (e.g., Covey-Crump, 1997). Estimates of the cooling rate for the PSZ at the end of our experiment (supporting information) suggest that the temperature fell below 150 °C after a period of less than 1 s. Calculations of the original grain size distribution within the analyzed areas prior to annealing were made using the equation for normal grain growth (e.g., Covey-Crump, 1997):
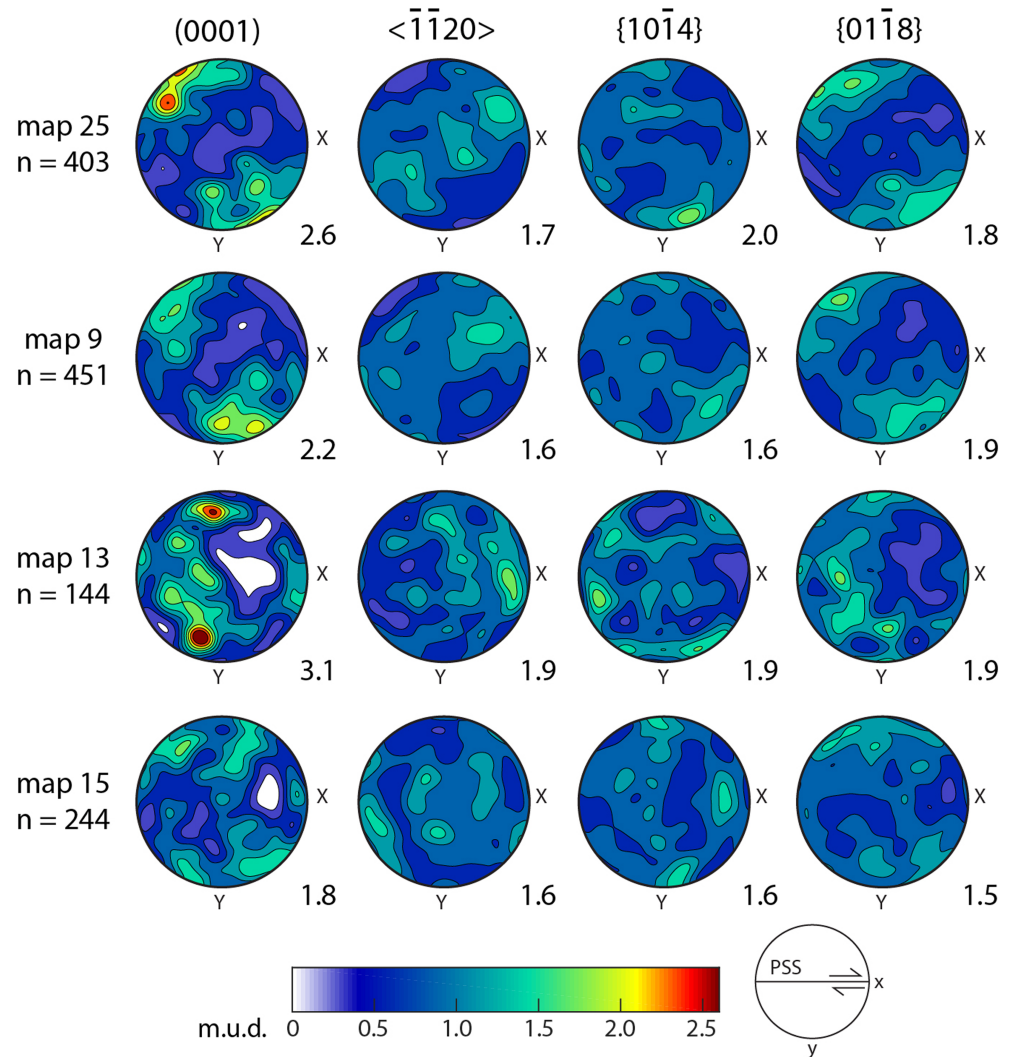
Figure 5. CPO data for calcite nanograins from the PSZ for the main crystallographic planes and directions. Values are scaled to the highest multiple of a uniform distribution (m.u.d.) value on (0001) for *map 25*. The PSS corresponds to the XZ plane, and the shear direction is parallel to the *x*-direction (see reference frame). Maximum m.u.d. values are annotated next to each pole figure.

$$d^{\frac{1}{n}} - d_0^{\frac{1}{n}} = kt$$

where d is the final grain size, d_0 is the initial grain size, k is a constant with an Arrhenius temperature dependence, n is a dimensionless constant that depends on the process controlling the grain growth, and t is the duration of the grain growth. Our calculations were done by assuming that the PSZ is composed of pure calcite (yellow bars in Figure 4a). Assuming 1 s of annealing, the calculations predict that individual grains may have grown by up to 30–50 nm. However, grain growth during annealing is hindered by the presence of impurities in calcite (i.e., partial exchange of Ca cations with Mg; Herwegh et al., 2003), as well as pinning of grain boundaries by second phases or pores (e.g., Covey-Crump, 1997; Davis et al., 2011). Grain growth rates in Mg-calcite and dolomite are lower than calcite by a factor of 10^3–10^4 (Davis et al., 2011; Herwegh et al., 2003). We suggest therefore that grain growth in the calcite-dolomite gouges was negligible (on the order of a few nanometers or less), and that the microstructures and grain sizes preserved in our sample are similar to those that were active during the high-velocity experiment. It is possible that extreme comminution and thermal decomposition generated amorphous carbon and CO_2 (e.g., Delle Piane et al., 2018; Demurtas et al., 2019; Spagnuolo et al., 2015), which could have enhanced grain growth rates. However, amorphous carbon was not identified during TKD analysis. The relatively high porosity of the PSZ, and
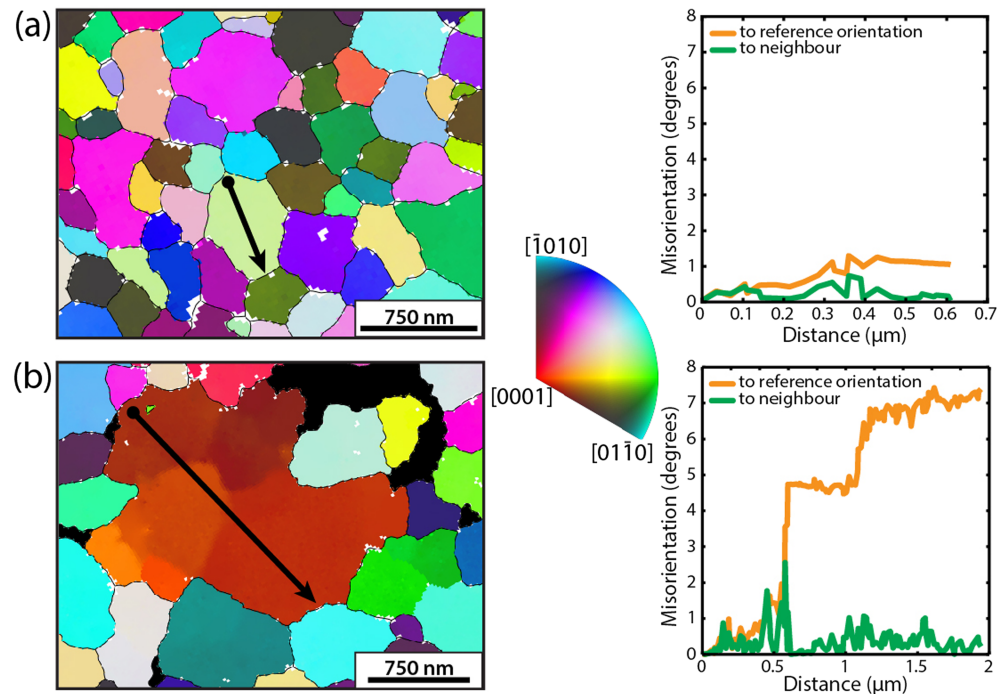
Figure 6. Maps (Inverse Pole Figure (IPFx); colored) and profiles (black arrows) showing intragranular misorientation of (a) nanograins within the ultrafine PSZ matrix (grain size < 800 nm) and (b) larger grains in the PSZ (grain size > 800 nm). Grain boundaries (misorientation angle $\geq 10°$) are shown as thin black lines on the maps. Subgrain boundaries are marked by stepwise increases in the progressive misorientation angle in respect to the reference orientation (i.e., beginning of the misorientation profile).

the unconfined nature of the gouge holder, also makes it likely that CO_2 produced, and measured, during the experiment was able to escape relatively easily (supporting information).

In our experiments, the PSZ contains grains that are dominantly 200–300 nm in size (Figure 4a). The aggregates have a foam-like microstructure (i.e., equant grains with relatively straight grain boundaries), triple junctions between roughly equant nanograins have approximately 120° dihedral angles, and quadruple junctions are common (Figures 2c and 6). These microstructures closely resemble those described by Schmid et al. (1977) and Walker et al. (1990), which formed during high-temperature deformation of calcite aggregates, interpreted to be the result of GSS creep during superplastic flow. The activation of grain boundary sliding aided by GSS creep in the ultrafine matrix of the PSZ is also supported by the presence of equant strain-free (i.e., low internal misorientation) grains in the matrix, usually confined to grain sizes of < 800 nm (Figure 6a; Poirier, 1985). However, GSI creep also seems to have been active during the experiment, because larger grains (> 800 nm) show irregular grain boundaries and contain subgrains (Figure 6b; Rutter, 1995). In addition, a weak CPO on (0001) is developed locally in some TKD maps (Figure 5). The similarity between the subgrain size in the larger grains and the size of grains in the surrounding ultrafine matrix suggests that the latter may have formed (at least partly) by subgrain rotation recrystallization. Pozzi et al. (2019) interpreted the progressive weakening of the CPO in calcite nanograins as evidence for a transition to a diffusion creep regime enhanced by grain size reduction and concomitant temperature increase. Previous work has suggested that deformation by diffusion creep accompanied by grain rotation may cause weakening — but not necessarily complete randomization — of any preexisting CPOs (Rutter et al., 1994; Taplin et al., 1979; Walker et al., 1990; Wheeler, 2009). However, deformation experiments in the GSS regime have also shown that CPO can develop under such conditions in fine-grained aggregates of calcite (Rutter et al., 1994), olivine (Fliervoet et al., 1999; Hansen et al., 2011), ice (Goldsby & Kohlstedt, 2001), anorthite (Barreiro et al., 2007), dolomite (Delle Piane et al., 2008), and calcite-dolomite mixtures (Delle Piane et al., 2009; Kushnir et al., 2015). In our experiments, the weak CPO may have been inherited from that developed in the bulk gouge as a result of early grain rotation and preferential fracturing along the *r*-rhomb calcite cleavage planes (Demurtas et al., 2019). Subsequently, extreme grain size reduction and temperature increase led to the
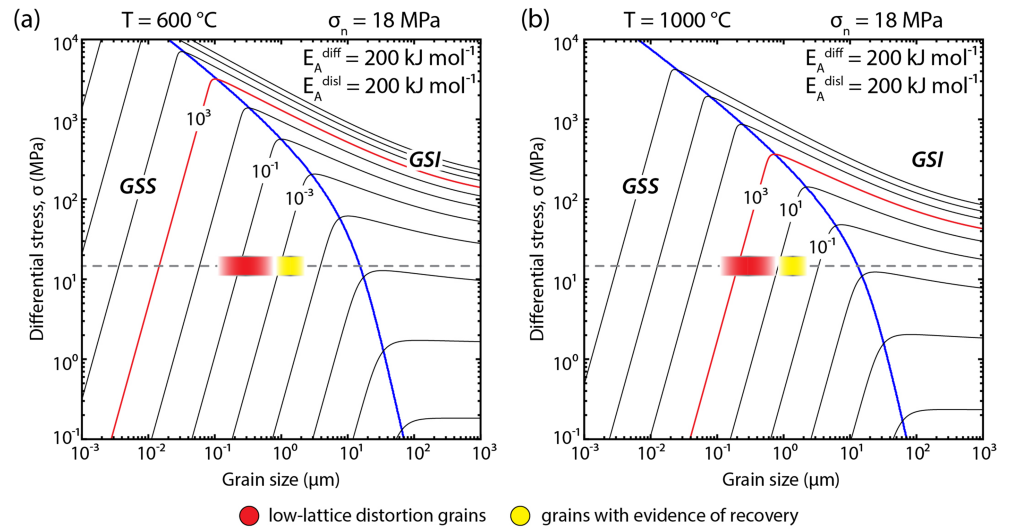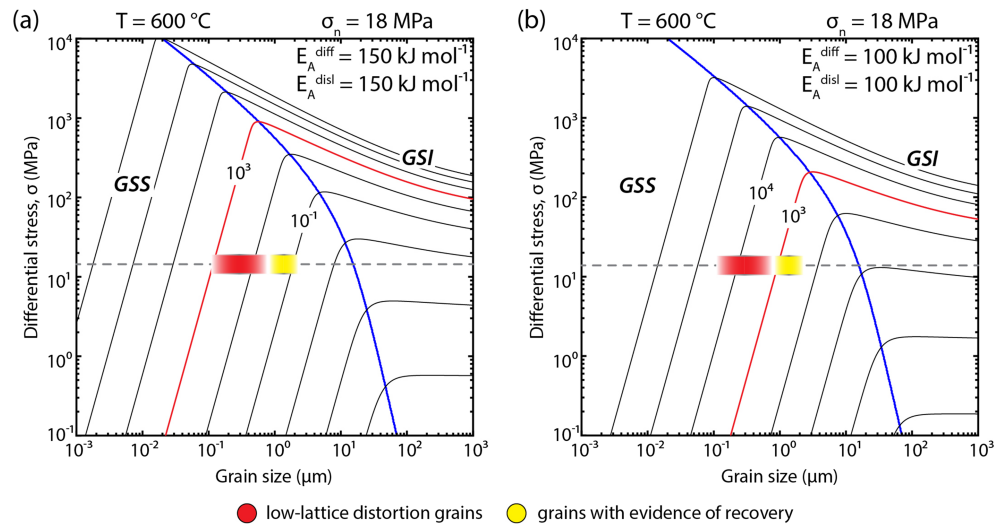
Figure 7. Deformation mechanism maps for calcite calculated for temperatures of (a) 600 °C and (b) 1000 °C. Flow laws from Renner et al. (2002) and Herwegh et al. (2003) were used for grain size insensitive (GSI) and grain size sensitive (GSS) creep, respectively. The blue line represents the field boundary after de Bresser et al. (1998, 2002). Strain rates are shown as labeled contours. The red contour represents the calculated strain rate of approximately 10^3 s for the PSZ in our experiment. The differential stress measured during steady state deformation is shown as dashed grey line. According to the deformation mechanism maps, in order to accommodate the estimated strain rates during deformation, the PSZ is supposed to reach a temperature of 1000 °C.

activation of GSS creep, with little to negligible change in the overall CPO in the PSZ. Given that the matrix in our experiment is dominated (90–95 vol %) by strain-free nanograins < 800 nm in size (Figure 4a), we infer that GSS creep mechanisms likely controlled the bulk rheology of the PSZ following dynamic weakening.

Figure 7 shows deformation mechanism maps calculated for calcite at temperatures of 600 °C and 1000 °C. The PSZ is assumed to be composed only of calcite, based on microstructural observations and mineralogical analysis showing a PSZ composed mainly of calcite and Mg-calcite with sparse dolomite grains. Flow laws for GSI and GSS creep were taken from Renner et al. (2002) and Herwegh et al. (2003), respectively. For GSI and GSS creep the stress exponent used were $n = 2$ and $n = 1.1$, respectively. The field boundary of de Bresser et al. (1998, 2002) corresponds to the stable grain sizes predicted to occur at the boundary between the diffusion and dislocation creep fields. The shear strain, γ, in the PSZ is calculated as $\gamma = {}^{r\theta}/_{2h}$, where r is the outer radius of the sample, θ is the angular displacement, and h is the average slip zone thickness (in our case $h = 100$ μm). The strain rate in the PSZ was calculated as $\dot{\gamma} = {}^{\Delta\gamma}/_{\Delta t}$, where Δt is the time interval considered and $\Delta\gamma$ is the shear strain accommodated in the PSZ during Δt. Calculated strain rates in the PSZ are $\dot{\gamma} \approx 6 \times 10^3$ s^{-1}, in accordance with previous estimates for similar experiments (e.g., De Paola et al., 2015). At the calculated temperatures, both the ultrafine matrix grains (red areas in Figure 7) and the larger grains containing subgrains (yellow areas in Figure 7) lie within the GSS field. The strain rates calculated for the observed grain size range in the deformation mechanism map at 600 °C are between 10^{-1} and 10^{-3}, which is a factor of 10^4–10^6 lower than the strain rate estimated to have occurred in the experiment. At 1000 °C, the strain rates are between 10^0 and 10^3, and the higher strain rates are consistent with the sizes of the nanograin population showing low values of intracrystalline distortion (Figure 7b). K-type thermocouples in the gouge layer measured peak temperatures of approximately 620 °C, consistent with our bulk temperature calculations (after Rice, 2006; see Text S2 in the supporting information for additional details). However, it is possible that significantly higher temperatures were reached locally in the PSZ in areas where heat dissipation was less efficient, or in areas where the temperature increase was enhanced by local processes such as flash heating along asperities. Temperatures of up to 1000 °C have previously been estimated for the PSZ in calcite gouges deformed at similar deformation conditions (De Paola et al., 2015; Pozzi et al., 2018).

If the peak temperature of the PSZ was indeed limited to 600 °C, the inconsistency between the estimated strain rate ($\dot{\gamma} = 6 \times 10^3$ s^{-1}) in the PSZ and the calculated strain rates in the deformation mechanism map (Figure 7a) might be related to the larger grain size at which the flow laws of Renner et al. (2002) and

Figure 8. Deformation mechanism maps for calcite calculated for temperatures of 600 °C and different activation energy for diffusion creep (E_A^{diff}) and dislocation creep (E_A^{disl}). The blue line represents the field boundary after de Bresser et al. (1998, 2002). Strain rates are shown as labeled contours. The red contour represents the calculated strain rate of approximately 10^3 s for the PSZ in our experiment. The differential stress measured during steady state deformation is shown as dashed grey line. By accounting for the nature of the nanoparticles, the reduction of E_A to creep allows the PSZ to deform at the calculated strain rates at temperatures of 600 °C.

Herwegh et al. (2003) were calculated (i.e., grains > 5–10 μm). In the case of nanoparticles, it has been demonstrated that grain size can have a major control on lowering the activation energy (E_A) required to activate creep and diffusion mechanisms (e.g., Cai et al., 2000; Guisbiers & Buchaillot, 2008; Li et al., 2004) or decomposition reactions (Yue et al., 1999). This grain size effect is a consequence of the excess energy stored on the nanograin surface (e.g., Asaro & Suresh, 2005; Yue et al., 1999) and the larger number of grain boundaries compared to a fine-grained aggregate. For nanoparticles produced by mechanical milling, the widespread presence of defects and internal plastic deformation in the nanoparticles is expected to result in a further lowering of E_A (Fisher, 1988). In Figure 8, we test two different scenarios where the E_A for diffusion (E_A^{diff}) and dislocation creep (E_A^{disl}) is reduced by 25% ($E_A = 150$ kJ/mol; Figure 8a) and 50% ($E_A = 100$ kJ/mol; Figure 8b) compared to the values of Renner et al. (2002) and Herwegh et al. (2003). Such reductions in E_A are consistent with previous observations of a decrease of E_A for thermal decomposition of calcite of 70–80 kJ/mol, corresponding to 35–40% of the reference value (Yue et al., 1999). By comparing the deformation mechanism maps in Figures 7 and 8, it is clear that a reduction in E_A due to the presence of nanograins could facilitate accommodation of very high strain rates ($\dot{\gamma} = 6 \times 10^3$ s^{-1}) by grain size sensitive flow, without necessarily having to invoke temperatures higher than approximately 600 °C. If this is the case, the activation of viscous deformation mechanisms during coseismic shearing could be expected to control the rheology of our experimental PSZ (also see Pozzi et al., 2018). Notably, the decomposition temperature is also expected to decrease in the presence of nanoparticles (Yue et al., 1999). As a consequence, particular care should be exercised when making peak temperature estimates based on the occurrence of decomposition products.

Collectively, our TKD observations provide quantitative microstructural and crystallographic data sets that are compatible with other observations of experimental carbonate slip zones (Verberne et al., 2013, 2014; De Paola et al., 2015; Green et al., 2015; Delle Piane et al., 2018; Pozzi et al., 2018, 2019). Our observations suggest that during high-velocity shearing the PSZ deforms mainly by GSS creep, possibly facilitated by a reduction in E_A within nanogranular aggregates, which allows high strain rates ($\dot{\gamma} = 6 \times 10^3$ s^{-1}) to be accommodated at moderate bulk temperatures (approximately 600 °C). Additionally, the presence of dolomite in the gouge mixture appears to have hindered significant grain growth after the experiment, resulting in final grain sizes and shapes that are likely to be similar to those active during high-velocity shearing. TKD allows quantitative investigation of the microstructure and crystallographic properties of nanograins in fault zones, and provides information that is complementary to TEM observations and EBSD data from coarser grain populations.

5. Conclusions

TKD was performed on the nanogranular principal slip zone of a calcite-dolomite gouge sheared experimentally at a maximum slip velocity of 1.2 m/s for 0.4 m displacement. X-ray powder diffraction shows that the slip zone consists of calcite, Mg-calcite, dolomite and periclase. Calculations of grain growth during annealing suggest that the post-mortem microstructures are representative of those active during high-velocity shearing. The TKD analysis reveals that the principal slip zone is recrystallized and composed of a population of equant grains approximately 200–300 nm in size with negligible intracrystalline misorientation, together with larger grains ($d > 800$ nm) that typically contain subgrains. Weak CPOs are defined by clustering of the calcite c axes in some areas of the PSZ. Together with published flow laws for calcite, these microstructural observations suggest that grain size sensitive creep in the ultrafine-grained PSZ matrix was the main deformation mechanism controlling slip zone rheology during high-velocity shearing. Grain size insensitive creep was also active and resulted in the formation of subgrains via subgrain rotation recrystallization inside the larger grains. A reduction of the activation energy (E_A) for creep in calcite nanograins would allow high (coseismic) strain rates to be accommodated at moderate bulk temperatures of approximately 600 °C.

References

Aretusini, S., Mittempergher, S., Plümper, O., Spagnuolo, E., Gualtieri, A. F., & Di Toro, G. (2017). Production of nanoparticles during experimental deformation of smectite and implications for seismic slip. *Earth and Planetary Science Letters*, *463*, 221–231. https://doi.org/10.1016/j.epsl.2017.01.048

Asaro, R. J., & Suresh, S. (2005). Mechanistic models for the activation volume and rate sensitivity in metals with nanocrystalline grains and nano-scale twins. *Acta Materialia*, *53*, 3369–3382. https://doi.org/10.1016/j.actamat.2005.03.047

Bachmann, F., Hielscher, R., & Schaeben, H. (2010). Texture analysis with MTEX—Free and open source software toolbox. *Solid State Phenomena*, *160*, 63–68. https://doi.org/10.4028/www.scientific.net/SSP.160.63

Bachmann, F., Hielscher, R., & Schaeben, H. (2011). Ultramicroscopy grain detection from 2d and 3d EBSD data—Specification of the MTEX algorithm. *Ultramicroscopy*, *111*, 1720–1733. https://doi.org/10.1016/j.ultramic.2011.08.002

Barreiro, J. G., Lonardelli, I., Wenk, H. R., Dresen, G., Rybacki, E., Ren, Y., & Tome, C. N. (2007). Preferred orientation of anorthite deformed experimentally in Newtonian creep. *Earth and Planetary Science Letters*, *264*(1-2), 188–207.

Barrett, S. (2015). Image SXM. Retrieved from http://www.ImageSXM.org.uk

Beeler, N. M., Tullis, T. E., Blanpied, M. L., & Weeks, J. D. (1996). Frictional behavior of large displacement experimental faults. *Journal of Geophysical Research*, *101*, 8697–8715. https://doi.org/10.1029/96JB00411

Boullier, A. M., & Gueguen, Y. (1975). SP-Mylonites: Origin of some mylonites by superplastic flow. *Contributions to Mineralogy and Petrology*, *50*, 93–104. https://doi.org/10.1007/BF00373329

Bunge, H. J. (1982). Fabric analysis by orientation distribution functions. *Tectonophysics*, *78*, 1.

Cai, B., Kong, Q. P., Lu, L., & Lu, K. (2000). Low temperature creep of nanocrystalline pure copper. *Materials Science and Engineering A*, *286*, 188–192. https://doi.org/10.1016/S0921-5093(00)00633-X

Chen, X., Madden, A. S., Bickmore, B. R., & Reches, Z. (2013). Dynamic weakening by nanoscale smoothing during high-velocity fault slip. *Geology*, *41*, 739–742. https://doi.org/10.1130/G34169.1

Chester, J. S., Chester, F. M., & Kronenberg, A. K. (2005). Fracture surface energy of the Punchbowl fault, San Andreas system. *Nature*, *437*, 133–136. https://doi.org/10.1038/nature03942

Covey-Crump, S. J. (1997). The normal grain growth behaviour of nominally pure calcitic aggregates. *Contributions to Mineralogy and Petrology*, *129*, 239–254. https://doi.org/10.1007/s004100050335

Davis, N. E., Newman, J., Wheelock, P. B., & Kronenberg, A. K. (2011). Grain growth kinetics of dolomite, magnesite and calcite: A comparative study. *Physics and Chemistry of Minerals*, *38*, 123–138. https://doi.org/10.1007/s00269-010-0389-9

de Bresser, J. H. P., Evans, B., & Renner, J. (2002). On estimating the strength of calcite rocks under natural conditions. In *Deformation mechanisms, rheology and tectonics: Current status and future perspectives*, *Geological Society of London, Special Publications* (Vol. 200, pp. 309–329).

de Bresser, J. H. P., Peach, C., Reijs, J., & Spiers, C. J. (1998). On dynamic recrystallization during solid-state flow: effects of stress and temperature. *Geophysical Research Letters*, *25*, 3457–3460.

De Paola, N., Hirose, T., Mitchell, T., Di Toro, G., Viti, C., & Shimamoto, T. (2011). Fault lubrication and earthquake propagation in thermally unstable rocks. *Geology*, *39*, 35–38. https://doi.org/10.1130/G31398.1

De Paola, N., Holdsworth, R. E., Viti, C., Collettini, C., & Bullock, R. (2015). Can grain size sensitive flow lubricate faults during the initial stages of earthquake propagation? *Earth and Planetary Science Letters*, *431*, 48–58. https://doi.org/10.1016/j.epsl.2015.09.002

Delle Piane, C., Burlini, L., & Kunze, K. (2009). The influence of dolomite on the plastic flow of calcite. Rheological, microstructural and chemical evolution during large strain torsion experiments. *Tectonophysics*, *467*, 145–166. https://doi.org/10.1016/j.tecto.2008.12.022

Delle Piane, C., Burlini, L., Kunze, K., Brack, P., & Burg, J. P. (2008). Rheology of dolomite: Large strain torsion experiments and natural examples. *Journal of Structural Geology*, *30*, 767–776. https://doi.org/10.1016/j.jsg.2008.02.018

Delle Piane, C., Piazolo, S., Timms, N. E., Luzin, V., Saunders, M., Bourdet, J., et al. (2018). Generation of amorphous carbon and crystallographic texture during low-temperature subseismic slip in calcite fault gouge. *Geology*, *42*.

Demurtas, M., Fondriest, M., Balsamo, F., Clemenzi, L., Storti, F., Bistacchi, A., & Di Toro, G. (2016). Structure of a normal seismogenic fault zone in carbonates: The Vado di Corno Fault, Campo Imperatore, central Apennines (Italy). *Journal of Structural Geology*, *90*, 185–206. https://doi.org/10.1016/j.jsg.2016.08.004

Demurtas, M., Smith, S. A., Prior, D. J., Spagnuolo, E., & Di Toro, G. (2019). Development of crystallographic preferred orientation during cataclasis in low-temperature carbonate fault gouge. *Journal of Structural Geology*. https://doi.org/10.1016/j.jsg.2019.04.015

Di Toro, G., Niemeijer, A., Tripoli, A., Nielsen, S., Di Felice, F., Scarlato, P., et al. (2010). From field geology to earthquake simulation: A new state-of-the-art tool to investigate rock friction during the seismic cycle (SHIVA). *Rendiconti Lincei*, *21*, 95–114. https://doi.org/10.1007/s12210-010-0097-x

Fisher, T. E. (1988). Tribochemistry. *Annual Review of Materials Science*, *18*, 303–323.

Fliervoet, T. F., Drury, M. R., & Chopra, P. N. (1999). Crystallographic preferred orientations and misorientations in some olivine rocks deformed by diffusion or dislocation creep. *Tectonophysics*, *303*, 1–27. https://doi.org/10.1016/S0040-1951(98)00250-9

Goldsby, D. L., & Kohlstedt, D. L. (2001). Superplastic deformation of ice: Experimental observations. *Journal of Geophysical Research*, *106*, 11,017–11,030.

Green, H. W., Shi, F., Bozhilov, K., Xia, G., & Reches, Z. (2015). Phase transformation and nanometric flow cause extreme weakening during fault slip. *Nature Geoscience*, *8*, 484–489. https://doi.org/10.1038/ngeo2436

Guisbiers, G., & Buchaillot, L. (2008). Size and shape effects on creep and diffusion at the nanoscale. *Nanotechnology*, *19*, 1–5. https://doi.org/10.1088/0957-4484/19/43/435701

Han, R., Hirose, T., & Shimamoto, T. (2010). Strong velocity weakening and powder lubrication of simulated carbonate faults at seismic slip rates. *Journal of Geophysical Research*, *115*, B03412. https://doi.org/10.1029/2008JB006136

Han, R., Hirose, T., Shimamoto, T., Lee, Y., & Ando, J. I. (2011). Granular nanoparticles lubricate faults during seismic slip. *Geology*, *39*, 599–602. https://doi.org/10.1130/G31842.1

Han, R., Shimamoto, T., Hirose, T., Ree, J.-H., & Ando, J. (2007). Ultralow friction of carbonate faults caused by thermal decomposition. *Science*, *316*, 878–881. https://doi.org/10.1126/science.1139763

Hansen, L. N., Zimmerman, M. E., & Kohlstedt, D. L. (2011). Grain boundary sliding in San Carlos olivine: Flow law parameters and crystallographic-preferred orientation. *Journal of Geophysical Research*, *116*, B08201. https://doi.org/10.1029/2011JB008220

Herwegh, M., Xiao, X., & Evans, B. (2003). The effect of dissolved magnesium on diffusion creep in calcite. *Earth and Planetary Science Letters*, *212*, 457–470. https://doi.org/10.1016/S0012-821X(03)00284-X

Humphreys, F. J., & Brough, I. (1999). High resolution electron backscatter diffraction with a field emission gun scanning electron microscope. *Journal of Microscopy*, *195*(Pt 1), 6–9.

Keller, R. R., & Geiss, R. H. (2012). Transmission EBSD from 10 nm domains in a scanning electron microscope. *Journal of Microscopy*, *245*, 245–251. https://doi.org/10.1111/j.1365-2818.2011.03566.x

Kushnir, A. R. L., Kennedy, L. A., Misra, S., Benson, P., & White, J. C. (2015). The mechanical and microstructural behaviour of calcite-dolomite composites: An experimental investigation. *Journal of Structural Geology*, *70*, 200–216. https://doi.org/10.1016/j.jsg.2014.12.006

Li, Y. J., Blum, W., & Breutinger, F. (2004). Does nanocrystalline Cu deform by Coble creep near room temperature? *Materials Science and Engineering A*, *387–389*, 585–589. https://doi.org/10.1016/j.msea.2003.11.086

Ma, K.-F., Tanaka, H., Song, S.-R., Wang, C.-Y., Hung, J.-H., Tsai, Y.-B., et al. (2006). Slip zone and energetics of a large earthquake from the Taiwan Chelungpu-fault Drilling Project. *Nature*, *444*, 473–476. https://doi.org/10.1038/nature05253

Mitchell, T. M., Smith, S. A. F., Anders, M. H., Di Toro, G., Nielsen, S., Cavallo, A., & Beard, A. D. (2015). Catastrophic emplacement of giant landslides aided by thermal decomposition: Heart Mountain, Wyoming. *Earth and Planetary Science Letters*, *411*, 199–207. https://doi.org/10.1016/j.epsl.2014.10.051

Niemeijer, A. R., Di Toro, G., Nielsen, S. B., & Di Felice, F. (2011). Frictional melting of gabbro under extreme experimental conditions of normal stress, acceleration, and sliding velocity. *Journal of Geophysical Research*, *116*, B07404. https://doi.org/10.1029/2010JB008181

Novellino, R., Prosser, G., Spiess, R., Viti, C., Agosta, F., Tavarnelli, E., & Bucci, F. (2015). Dynamic weakening along incipient low-angle normal faults in pelagic limestones (southern Apennines, Italy). *Journal of the Geological Society*, *172*(3), 283–286.

Piazolo, S., Kaminsky, F. V., Trimby, P., Evans, L., & Luzin, V. (2016). Carbonado revisited: Insights from neutron diffraction, high resolution orientation mapping and numerical simulations. *Lithos*, *265*, 244–256. https://doi.org/10.1016/j.lithos.2016.09.011

Pittarello, L., Di Toro, G., Bizzarri, A., Pennacchioni, G., Hadizadeh, J., & Cocco, M. (2008). Energy partitioning during seismic slip in pseudotachylyte-bearing faults (Gole Larghe Fault, Adamello, Italy). *Earth and Planetary Science Letters*, *269*, 131–139. https://doi.org/10.1016/j.epsl.2008.01.052

Poirier, J.-P. (1985). *Creep of crystals: High-temperature deformation processes in metals, ceramics and minerals*. London, New York: Cambridge University Press.

Pozzi, G., De Paola, N., Nielsen, S. B., Holdsworth, R. E., & Bowen, L. (2018). A new interpretation for the nature and significance of mirror-like surfaces in experimental carbonate-hosted seismic faults. *Geology*, *46*, 583–586. https://doi.org/10.1130/G40197.1

Pozzi, G., De Paola, N., Holdsworth, R. E., Bowen, L., Nielsen, S. B., & Dempsey, E. D. (2019). Coseismic ultramylonites: An investigation of nanoscale viscous flow and fault weakening during seismic slip. *Earth and Planetary Science Letters*, *516*, 164–175.

Prior, D. J., Boyle, A. P., Brenker, F., Cheadle, M. C., Day, A., Lopez, G., et al. (1999). The application of electron backscatter diffraction and orientation contrast imaging in the SEM to textural problems in rocks. *American Mineralogist*, *84*, 1741–1759. https://doi.org/10.2138/am-1999-11-1204

Prior, D. J., Mariani, E., & Wheeler, J. (2009). *EBSD in the Earth sciences: Applications, common practice, and challenges. Electron Backscatter Diffraction in Materials Science* (pp. 345–360). Boston, MA: Springer. https://doi.org/10.1007/978-0-387-88136-2

Reches, Z. E., & Lockner, D. A. (2010). Fault weakening and earthquake instability by powder lubrication. *Nature*, *467*(7314), 452.

Renner, J., Evans, B., & Siddiqi, G. (2002). Dislocation creep of calcite. *Journal of Geophysical Research*, *107*(B12), 2364. https://doi.org/10.1029/2001JB001680

Rice, J. R. (2006). Heating and weakening of faults during earthquake slip. *Journal of Geophysical Research*, *111*, B05311. https://doi.org/10.1029/2005JB004006

Rowe, C. D., & Griffith, W. A. (2015). Do faults preserve a record of seismic slip: A second opinion. *Journal of Structural Geology*, *78*, 1–26. https://doi.org/10.1016/j.jsg.2015.06.006

Rutter, E. H. (1995). Experimental study of the influence of stress, temperature, and strain on the dynamic recrystallization of Carrara marble. *Journal of Geophysical Research*, *100*(B12), 24,651–24,663.

Rutter, E. H., Casey, M., & Burlini, L. (1994). Preferred crystallographic orientation development during the plastic and superplastic flow of calcite rocks. *Journal of Structural Geology*, *16*, 1431–1446. https://doi.org/10.1016/0191-8141(94)90007-8

Sammis, C. G., & Ben-Zion, Y. (2008). Mechanics of grain-size reduction in fault zones. *Journal of Geophysical Research*, *113*, B02306. https://doi.org/10.1029/2006JB004892

Samtani, M., Dollimore, D., & Alexander, K. S. (2002). Comparison of dolomite decomposition kinetics with related carbonates and the effect of procedural variables on its kinetic parameters. *Thermochimica Acta*, *393*, 135–145.

Schmid, S. M., Boland, J. N., & Paterson, M. S. (1977). Superplastic flow in finegrained limestone. *Tectonophysics*, *43*, 257–291. https://doi.org/10.1016/0040-1951(77)90120-2

Siman-Tov, S., Aharonov, E., Sagy, A., & Emmanuel, S. (2013). Nanograins form carbonate fault mirrors. *Geology*, *41*, 703–706. https://doi.org/10.1130/G34087.1

Smeraglia, L., Bettucci, A., Billi, A., Carminati, E., Cavallo, A., Di Toro, G., et al. (2017). Microstructural evidence for seismic and aseismic slips along clay-bearing, carbonate faults. *Journal of Geophysical Research: Solid Earth*, *122*, 1–21. https://doi.org/10.1002/2017JB014042

Smeraglia, L., Billi, A., Carminati, E., Cavallo, A., & Doglioni, C. (2017). Field- to nano-scale evidence for weakening mechanisms along the fault of the 2016 Amatrice and Norcia earthquakes, Italy. *Tectonophysics*, *712–713*, 156–169. https://doi.org/10.1016/j.tecto.2017.05.014

Smith, S. A. F., Di Toro, G., Kim, S., Ree, J.-H., Nielsen, S. B., Billi, A., & Spiess, R. (2013). Coseismic recrystallization during shallow earthquake slip. *Geology*, *41*, 63–66. https://doi.org/10.1130/G33588.1

Smith, S. A. F., Griffiths, J. R., Fondriest, M., & Di Toro, G. (2017). "Coseismic foliations" in gouge and cataclasite: Experimental observations and consequences for interpreting the fault rock record. In M. Y. Thomas, T. M. Mitchell, & H. S. Bhat (Eds.), *Fault zone dynamic processes: Evolution of fault properties during seismic rupture*, *Monograph of the American Geophysical Union* (Vol. 227, pp. 81–102).

Smith, S. A. F., Nielsen, S., & Di Toro, G. (2015). Strain localization and the onset of dynamic weakening in calcite fault gouge. *Earth and Planetary Science Letters*, *413*, 25–36. https://doi.org/10.1016/j.epsl.2014.12.043

Spagnuolo, E., Plümper, O., Violay, M. E. S., Cavallo, A., & Di Toro, G. (2015). Fast-moving dislocations trigger flash weakening in carbonate-bearing faults during earthquakes. *Scientific Reports*, *5*. https://doi.org/10.1038/srep16112

Stojic, A. N., & Brenker, F. E. (2010). Argon ion slicing (ArIS): A new tool to prepare super large TEM thin films from Earth and planetary materials. *European Journal of Mineralogy*, *22*, 17–21. https://doi.org/10.1127/0935-1221/2009/0022-2004

Taplin, D. M. R., Dunlop, G. L., & Langdon, T. G. (1979). Flow and failure of superplastic materials. *Annual Review of Materials Science*, *9*, 151–189.

Tisato, N., Di Toro, G., De Rossi, N., Quaresimin, M., & Candela, T. (2012). Experimental investigation of flash weakening in limestone. *Journal of Structural Geology*, *38*, 183–199. https://doi.org/10.1016/j.jsg.2011.11.017

Trimby, P. W. (2012). Orientation mapping of nanostructured materials using transmission Kikuchi diffraction in the scanning electron microscope. *Ultramicroscopy*, *120*, 16–24. https://doi.org/10.1016/j.ultramic.2012.06.004

Trimby, P. W., Cao, Y., Chen, Z., Han, S., Hemker, K. J., Lian, J., et al. (2014). Characterizing deformed ultrafine-grained and nanocrystalline materials using transmission Kikuchi diffraction in a scanning electron microscope. *Acta Materialia*, *62*, 69–80. https://doi.org/10.1016/j.actamat.2013.09.026

Verberne, B. A., de Bresser, J. H. P., Niemeijer, A. R., Spiers, C. J., de Winter, D. A. M., & Plümper, O. (2013). Nanocrystalline slip zones in calcite fault gouge show intense crystallographic preferred orientation: Crystal plasticity at subseismic slip rates at 18–150 °C. *Geology*, *41*, 863–866. https://doi.org/10.1130/G34279.1

Verberne, B. A., Plümper, O., de Winter, M. D. A., & Spiers, C. J. (2014). Superplastic nanofibrous slip zones control seismogenic fault friction. *Science*, *346*, 1342–1344. https://doi.org/10.1126/science.1259003

Walker, A. N., Rutter, E. H., & Brodie, K. H. (1990). Experimental study of grain-size sensitive flow of synthetic, hot-pressed calcite rocks. *Geological Society, London, Special Publications*, *54*, 259–284. https://doi.org/10.1144/gsl.sp.1990.054.01.24

Wheeler, J. (2009). The preservation of seismic anisotropy in the Earth's mantle during diffusion creep. *Geophysical Journal International*, *178*, 1723–1732. https://doi.org/10.1111/j.1365-246X.2009.04241.x

Wilson, B., Dewers, T. A., Reches, Z., & Brune, J. (2005). Particle size and energetics of gouge from earthquake rupture zones. *Nature*, *434*, 749–752. https://doi.org/10.1038/nature03433

Yao, L., Ma, S., Niemeijer, A. R., Shimamoto, T., & Platt, J. D. (2016). Is frictional heating needed to cause dramatic weakening of nanoparticle gouge during seismic slip? Insights from friction experiments with variable thermal evolutions. *Geophysical Research Letters*, *43*, 6852–6860. https://doi.org/10.1002/2016GL069053

Yue, L., Miao, S., & Zhude, X. (1999). The decomposition kinetics of nanocrystalline calcite. *Thermochimica Acta*, *335*, 121–126. https://doi.org/10.1016/S0040-6031(99)00174-4

Yund, R. A., Blanpied, M. L., Tullis, T. E., & Weeks, J. D. (1990). Amorphous material in high strain experimental fault gouges. *Journal of Geophysical Research*, *95*(B10), 15,589–15,602.